Orogen-parallel, active left-slip faults in the Eastern Himalaya: Implications for the growth mechanism of the Himalayan Arc

Dewei Li [a], An Yin [b,c,*]

[a] Faculty of Earth Sciences and Center for Tibetan Plateau Studies, China University of Geosciences (Wuhan), Wuhan, Hubei Province 430074, China
[b] Department of Earth and Space Sciences and Institute of Geophysics and Planetary Physics, University of California, Los Angeles, CA 90095-1567, USA
[c] Center for Tibetan Plateau Research and Structural Geology Group, School of Earth Sciences and Environments, China University of Geosciences (Beijing), Beijing, China

ARTICLE INFO

ABSTRACT

One of the key issues about the evolution of the Himalayan orogen is how its map-view curvature has changed with time. Some researchers propose that the arc curvature has decreased due to arc-perpendicular rifting while others suggest that it has increased due to arc-parallel strike–slip faulting. To quantify this problem we conducted field mapping, geomorphologic analysis of active structures, and dating of Pliocene–Quaternary sedimentary units in southeastern Tibet. This study reveals the existence of a ~100-km wide and >500-km long, east-striking left-slip fault zone in the eastern Himalaya. The left-slip faults initiated prior to 3–4 Ma and have a total left-slip rate of 4–8 mm/yr across the fault zone. Although the left-slip rate in the eastern Himalaya is broadly comparable to the right-slip rate across the western Himalayan arc, the distributed and short-segmented geometry of left-slip faulting in the eastern Himalaya contrasts sharply to the discrete geometry of right-slip faulting in the western Himalaya. The different geometry may have resulted from an earlier initiation and a greater magnitude of fault motion on the right-slip faults, which implies that asymmetric eastward extrusion of western Tibet across the Himalayan arc was a dominant process in the earlier Himalayan history. This was replaced by oroclinal bending since 4 Ma, producing symmetric right-slip and left-slip faulting in the western and eastern Himalaya, respectively.

© 2008 Elsevier B.V. All rights reserved.

1. Introduction

Researchers have long argued that the Himalayan arc is expanding radially outward relative to the fixed and rigid Indian craton as indicated by arc-perpendicular convergence (Seeber and Armbruster, 1984; Klootwijk et al., 1985; Molnar and Lyon-Caen, 1989). Arc expansion may be accomplished by continuum deformation (Seeber and Armbruster, 1984) or by lateral extrusion of Tibet (Amijo et al., 1986); the latter is associated with en echelon right-slip faulting and geometrically linked north-trending rifting. A consequence of arc expansion is a decrease in arc curvature with time (Fig. 1A). Alternatively, the curvature of the Himalayan arc may have increased with time via oroclinal bending accommodated by coeval right- and left-slip faulting in the western and eastern Himalaya, respectively (Ratschbacher et al., 1992, 1994) (Fig. 1A). Although Cenozoic left-slip faults were recognized locally near the eastern Himalayan syntaxis (Burg et al., 1998; Ding et al., 2001), along the Indus–Tsangpo suture (Yin et al., 1994) and across the Yadong–Guru rift zone (Li, 1992; Ratschbacher et al., 1994) (Fig. 2), the lack of active left-slip faulting in the eastern Himalaya has cast doubts on the impor-

tance of oroclinal bending in the Himalayan development and its active tectonics (e.g., Armijo et al., 1989). In this study, we present new structural and geochronologic results on a series of active left-slip faults across the eastern Himalaya near Dinggye area (87°E) in southeastern Tibet (Figs. 2 and 3). Our work constrains the slip rates of the left-slip fault zone that allow us to compare them with rates of the right-slip faults in the western Himalaya. We detail our study below.

2. Methods

2.1. Field mapping

We conducted field mapping at scales of 1:50,000 and 1:100,000 as part of a comprehensive mapping program sponsored by the Chinese Geological Survey. We complemented our mapping with analysis of satellite images mostly obtained from Google Earth.com that facilitated greatly our mapping efforts of Pliocene–Quaternary units.

2.2. Geochronology

In order to constrain slip rates of major active faults, we dated a series of Pliocene-Quaternary units. The dating methods include the electron spinning resonance (ESR) optical dating of quartz, optically stimulated luminescence (OSL) dating of feldspar, and radiocarbon dating of organic materials in lake deposits (Tables 1–3).

* Corresponding author. Department of Earth and Space Sciences and Institute of Geophysics and Planetary Physics, University of California, Los Angeles, CA 90095-1567, USA.
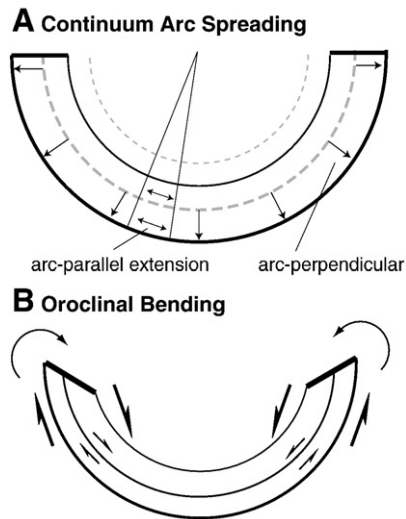   E-mail address: yin@ess.ucla.edu (A. Yin).

Fig. 1. Two end member mechanisms for variation of Himalayan-arc curvature: (A) continuum arc spreading and (B) oroclinal bending.

We carried out ESR dating at the Qingtao Analytical Facility Center for Marine Geology Research, which is administered by the Chinese Ministry of Land and Resources. All measurements were conducted at room temperature using an EMX Bruker ECS-160 ESR spectrometer with an alternating time of 5.12 μs, a time constant at 40.96 μs, and an incident microwave power of 1.0 mW. The sweep width was 5 mT with the center magnetic field at 348 mT. The uncertainty of the age estimate is between 10% and 15% (2σ). We use an uncertainty of 15% for all ESR ages reported in this study (Table 1). One may refer to Beerten and Stesmans (2007) and references therein for further information with regard to the method.

Samples for OSL dating were collected using concealed alloy tubes and were analyzed at the China Seismology Bureau in Beijing. The analytical procedure follows that of Wintle (1997). We separated fine-grained (4–11 μm) feldspar fractions by repeated Stokes settling with the presence of 20% HCl. We also used H_2O_2 to remove organic materials in the samples. The resulting fine-grained components were deposited from acetone onto aluminum discs with a 1-cm diameter. About 50 aliquots were prepared for each sample and were normalized by 0.1 s for infrared stimulated emission (IRSL) analysis. Within a given set of discs, normalization factors vary over a range of ∼ 8%. Depletion of the natural signal by short shine was about 1.8%. Halves of the sample discs were bleached by sunlight with a yellow filter for 90 min to simulate the *in situ* exposure conditions. Both natural and bleached aliquots were irradiated in preparation for analysis using the regeneration protocol of Prescott and Fox (1993). The equivalent doses (De in Table 2) were measured on Daybreak equipment while the irradiation dose rates were calibrated at the Chinese National Bureau of Technological Standards. After normalization of short shine, the discs were preheated at 220°C for 300 s to reduce the possibility of short-term thermal fading. The detection filter was BG39 plus 7–59. We used the slide procedure with a linear or saturating exponential fit of Prescott and Fox (1993) to determine the paleo-dose values of De (Table 2). As our samples were collected from lacustrine and alluvial deposits, we used different water contents to simulate possible absorption of sunlight by water during deposition of our measured samples. Because water typically filters out long- and short-wavelength components, the penetrating sunlight typically has a wavelength of 500–700 nm. As a result, we performed fading experiments by placing a yellow filter over each sample that allows sunlight with >510-nm wavelength to penetrate the filter. Our fading experiments over each sample lasted for over three hours. Dose rates contributed from 238U, 232Th and 40 K were obtained from laboratory analyses. Potassium was measured by X-ray fluorescence at the Analytical Facility Center of the Chinese Ministry of Nuclear Industry,

with an analytical uncertainty of <10%, while U and Th were measured by thick-source alpha counting (TSAC) combined with delayed neutron analysis using the Daybreak equipment. For all the measurements, the alpha-particle count ranges from 400 to 1100, with a frequency of 2–5 per millisecond. For all of the samples, Th contents are rather low (Table 2). We used the quantitative relationships proposed by Aitken (1985) to calculate the content of U, Th and K in feldspar. We calculated cosmogenic contribution to the dose rates using the procedure of Hutton and Prescott (1992).

A problem with the above dose-rate estimates contributed by decay of 238U, 232Th and 40K is that they were measured under the current water contents of the samples, which are lower than the water contents of the samples at the time of their deposition. As all of the samples were collected from water-laid sediments, corrections for the effect of water on alpha, beta, and gamma decays are necessary. In our estimates, we assume a water content of 5% or 10% and a saturation fraction of 0.5 or 1. All of the OSL ages discussed below are average values obtained from variable conditions discussed above (also see Table 2).

Radiocarbon age analyses were carried out using an accelerator mass spectrometer at Beijing University in China. First, we cleaned the samples by removing potentially contaminating materials such as modern plant fragments and tree roots. We then sieved the samples to obtain fine-grained components. The remaining sample materials were boiled in 2% NaOH solution for separation of insoluble matter and humic acid derivatives and rinsed using 10% hydrochloric acid. The final products were drived and burned to carbon dioxide from which benzene was synthesized for liquid scintillation spectrometry in Quantilus™ counters at the China Seismology Bureau, Beijing. The results of radiocarbon dating are shown in Table 3.

3. Stratigraphy of Pliocene–Quaternary units

The Dinggye area exposes the Gongzuo and Comuzhelin basins in the south and north bounded by active east-striking faults (Fig. 3). In the Gongzuo basin, Pliocene–Quaternary units include modern glacial-alluvial deposits (unit T0 in Fig. 4), terrace-forming glacial, alluvial and lacustrine deposits (units T1, T2, and T3 in Fig. 4), and fluvial-lacustrine sediments (Tla in Fig. 4). The T3 unit is the oldest mapped terrace sequence in the Gongzuo basin, exposed at the highest elevations relative to other mapped terraces (generally >4800 m and in places >5100 m). Its deposits, >150-m thick, comprise well- bedded and consolidated cyclic beds of pebble sandstone, siltstone and claystone. The pebbles are mostly limestone with minor sandstone derived from the Paleozoic Tethyan Himalayan Sequence (THS) in the hanging wall of the South Tibet Detachment (STD) (Fig. 3). ESR optical dating of quartz from a sample in the lower part of the T3 sequence yields a Pliocene age of 3.41±0.5 Ma (sample 1 in Fig. 4). We interpret the T3 unit to have been deposited in a glacial–lacustrine setting.

The >80-m thick T2 unit is composed of conglomerate, pebble sandstone, siltstone and claystone in the southern Gongzuo basin (Fig. 4). Cobbles are mostly sandstone, slate and limestone derived from the THS in the lower part of the unit and high-grade metamorphic clasts from the Greater Himalayan Crystalline Complex (GHC) below the STD (Fig. 4) in the upper part of the unit. We further divide the T2 unit into the T2a and T2b units, with the former as the most dominant subunit in the area. The T2a and T2b units are divided by a regionally extensive erosion surface. We analyzed two samples from the lower part of the T2a unit for their depositional ages, which yield an ESR age of 503.2±62 ka (sample 2 in Fig. 4) and an OSL age of 342.5±48 ka (sample 3 in Fig. 4). A sample from the base of unit T2b immediately above the erosion surface yields an OSL age of 173.1±18.6 ka (sample 4 in Fig. 4). Similar to the T3 unit, we interpret the T2 unit to have been deposited in a glacial–lacustrine setting.

The T1 unit is mainly composed of clay and silt interlayered with conglomerate. Cobbles in the conglomerate beds are mostly orthogneiss, schist and leucogranite derived from the GHC in the STD footwall (Fig. 3). We interpret the T1 unit to have been deposited in a
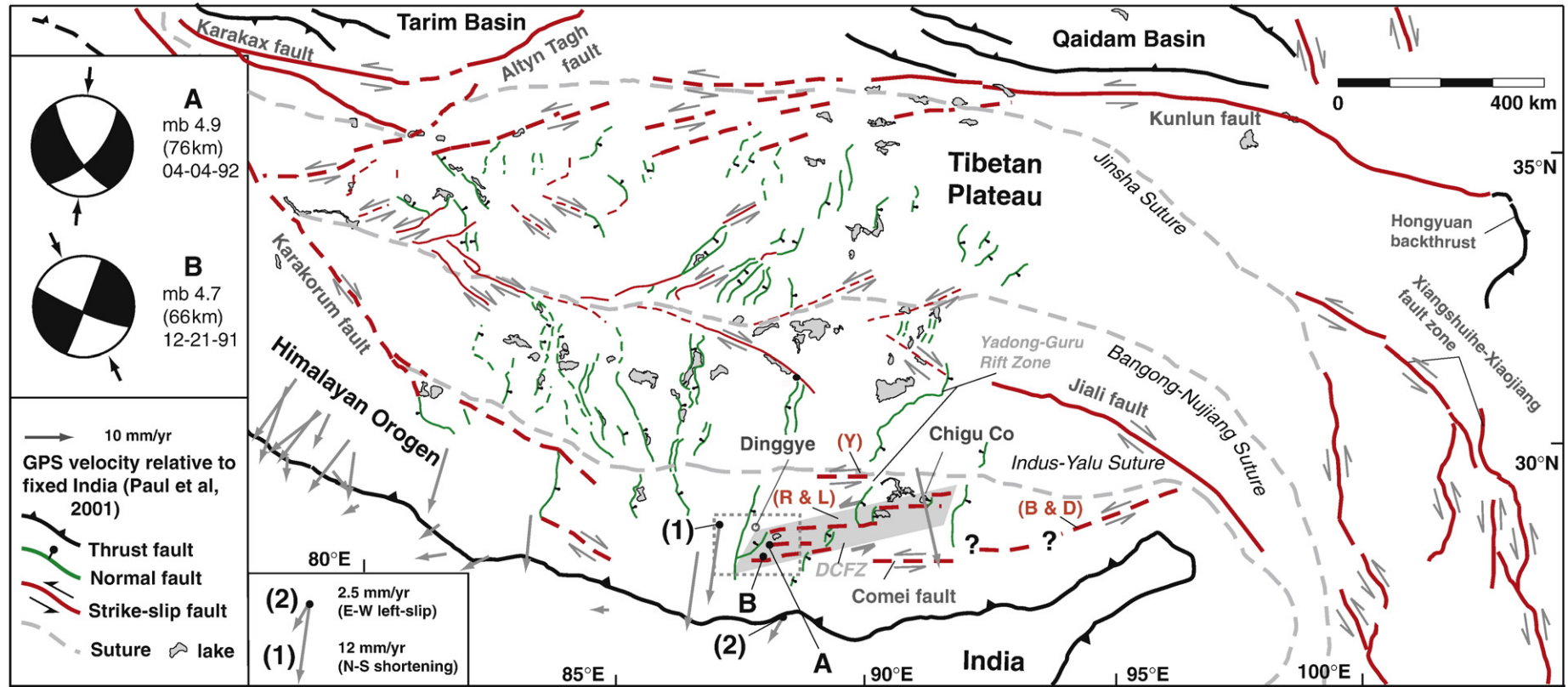
Fig. 2. Active fault map of the Tibetan plateau and the Himalaya orogen, modified from Taylor et al. (2003). Orogen-parallel left-slip faults in the eastern Himalaya were observed from this study (the Dinggye–Chigu fault zone), Yin et al. (1994) along the Indus–Tsangpo suture (shown as Y), Ratschbacher et al. (1994) and Li (1992) (shown as R and L) across the southern Yadong–Guru rift zone, and Ding et al. (2001) and Burg et al. (1998) near the eastern Himalayan syntaxis (shown as R and B). Points (A) and (B) are locations of two lower crustal strike–slip earthquakes in the study areas, with the focal mechanisms and depths after Priestley et al. (2007). Points (1) and (2) are GPS velocity vectors near our study area after Paul et al. (2001). The velocity gradient between the two points indicates ~2.5 mm/yr east-west left-slip faulting and ~12 mm/yr north-south contraction.
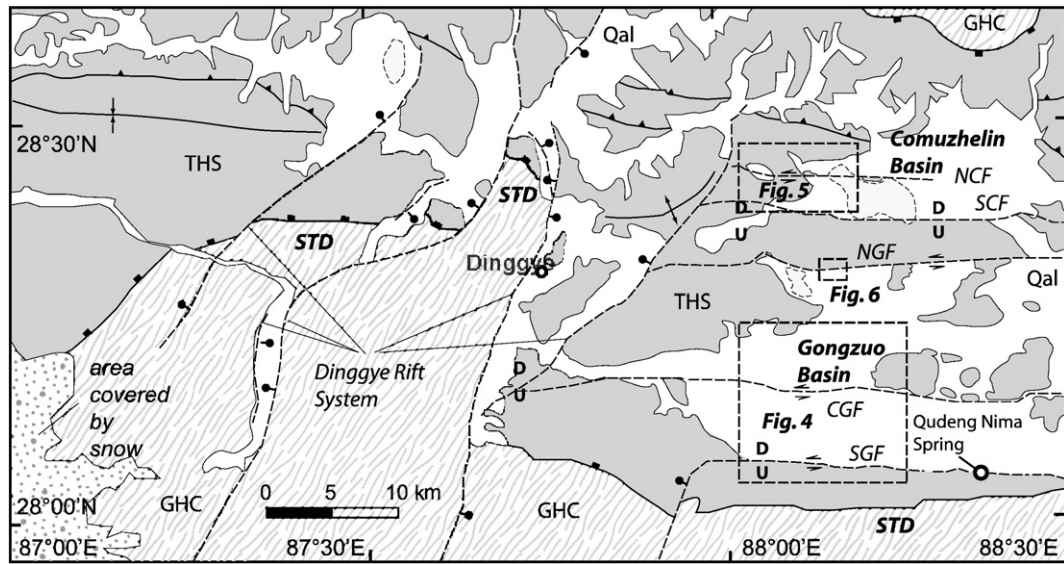
Fig. 3. Simplified geologic map of the Dinggye area based on Pan et al. (2004) and our mapping. Map units: GHC, Greater Himalayan Crystalline Complex; THS, Tethyan Himalayan Sequence; Qal, Quaternary deposits; STD, South Tibet Detachment; SGF, South Gongzuo fault; CGF, Central Gongzuo fault; NGF, North Gongzuo fault; SCF, South Comuzhelin fault; NCF, North Comuzhelin fault. "U" represents up-thrown fault block and "D" represents down-thrown fault block.

distal facies of a glacial–lacustrine system. One sample from the T1 sequence yields an OSL age of 41.4±3.5 ka (sample 5 in Fig. 4).

We group all modern glacial, alluvial, fluvial and lacustrine deposits together as the T0 unit. Glacial deposits are near the mountain front in the south, which contain boulders up to several meters in the longest dimension. Based on cross-cutting relationships, the T0 unit can be further divided into an older (T0a) and a younger sequence (T0b). We obtained an OSL age of 24.6±2.6 ka from the younger T0b unit north of the Central Gongzuo fault (sample 6 in Fig. 4).

In the Comuzhelin basin located north of the Gongzuo basin (Fig. 3), we have mapped four Quaternary units: Q1 is the oldest unit and represents older fan deposits, Q2 presents regressive-shoreline deposits, Q3 represents younger fan deposits postdating the regressive shoreline sequences, and Q4 represents modern stream deposits. The older alluvial fan unit (sample 7 from unit Q1a in Fig. 5) yields an OSL age of 21.0±2.0 ka. We obtained three radiocarbon ages from a 2-m-thick Q2 lacustrine sequence from a regressive shoreline sequence immediately above the current lake level (sample 8 in Fig. 5). As regressive shorelines retreat from higher to lower elevations during a progressive decrease in lake levels, the lowest shorelines should have formed during the terminal stage of shoreline retreat. Radiocarbon dating yields an age of 1290±55 yr for sample 8a collected from the uppermost part of the sequence, an age of 3445±70 yr for sample 8b from the middle part of the sequence, and an age of 3670±320 yr for sample 8c from the lowest part of the sequence. The above ages are consistent with their respective stratigraphic relationships and constrain the youngest regressive lake shoreline deposits to be between 21 ka and 1.3 ka.

4. Structures

The South Tibet Detachment (STD) of Burchfiel et al. (1992) juxtaposes Cambrian phyllite and Ordovician limestone of the THS over gneisses, schist, quartzite, and marble of the GHC (Fig. 3). The structure is cut by the north-striking Dinggye rift system (Fig. 3), suggesting that it is

no longer active. The Comuzhelin and Gongzuo basins are bounded by several east-trending faults. The South Gongzuo fault (SGF) is a range-bounding structure, marking the southern margin of the Gongzuo basin. The structure separates the high ranges (mostly >5100 m) in the south from the Gongzuo basin with an average elevation of ~4500 m in the north. The trace of the topographic front is generally straight in the east (Fig. 3) but irregular in the west (Fig. 4). Besides morphological expressions for the existence of an active fault, numerous springs also occur along the fault trace, with the Qudeng Nima Spring (Fig. 3) as the most prominent one having a daily flux of ~80 ton. The recent fault activity on the South Gongzuo fault is also indicated by left-lateral deflection of north-flowing stream channels, ranging from 500 m to 3500 m. We interpret the stream deflection to result from left-slip motion on the fault (Fig. 3). We note that several short streams do not display left-lateral deflection across the South Gongzuo fault, possibly due to their deposition after the last fault motion.

The Central Gongzuo fault (CGF) truncates several alluvial fans (T0a) and bounds an active fluvial-lacustrine depo-center to the north (Fig. 4). The fault offsets a stream channel for ~1100 m left-laterally (Fig. 4). Several sharp linear scarps are exposed along the fault trace that is locally covered by younger alluvial deposits (unit T0b) (Fig. 4). The age of the post-faulting fan deposits may be estimated by the age of a correlative fan sequence directly to the north at ~25 ka (sample 6 in Fig. 4). This implies that the Central Gongzuo fault has been inactive in the past 25 ka.

Short segments of fault scarps cutting T2 and T3 fan surfaces are also exposed south of the Central Gongzuo fault; motion on these faults has placed T3 terrace deposits against T2 deposits (Fig. 4). The general west-northwest trend of these minor structures is oblique to the east-trending Central Gongzuo fault, and we interpret them as en echelon contractional structures associated with broad left-slip shear deformation. In addition to left-slip motion, the Central Gongzuo fault also has a dip–slip component with the north side of the fault down, controlling the modern depo-center of the Gongzuo basin.

The North Gongzuo fault (NGF) bounds the northern margin of the Gongzuo basin in the south and offsets alluvial fans, stream channels, and four sequences of terrace deposits left-laterally (Figs. 3 and 6). The riser bounded by terrace horizons T3 and T2 is offset ~380 m; the riser bounded by terrace horizons T2 and T1 is offset ~180 m; finally the riser bounded by terrace horizons T1 and T0 is offset ~85 m. In addition to the left-slip motion, the fault also has a minor dip–slip component, juxtaposing the T4 terrace deposits against the T3 deposits with the south side of the fault down (Fig. 6).

Table 1
ESR dating results

Sample number	U (ppm)	Th (ppm)	K2O (%)	AD (Gy)	Age (ka)
(1)	1.77	13.05	1.76	1554.9	503.2±62
(2)	1.41	9.15	1.11	7127.6	3410±410

Table 2
OSL dating results based on IRSL analysis

Sample number in Figs. 4 and 5	Th (ppm)	U (ppm)	K (%)	Palaeo-dose (Gy)	Plateau (s)	Water content (%)	Saturation fraction	A value	Dose rate (Gy/ka)	OSL age (ka)	Mean age (ka)
(7)	0.021±0.021	0.165±0.022	2.66	86.4±5.7	1–72	5.0	0.5	0.133±0.004	3.439	19.9±1.9	21.0±2.0
						5.0	1.0		3.259	21.0±2.0	
						10.0	0.5		3.259	21.0±2.0	
						10.0	1.0		3.085	22.2±2.1	
(6)	0.005	0.114±0.013	3.80	96.3±7.9	10–50	5.0	0.5	0.104±0.002	3.991	24.1±2.5	24.6±2.6
						5.0	1.0		3.935	24.5±2.6	
						10.0	0.5		3.935	24.5±2.6	
						10.0	0.5		3.629	25.2±2.6	
(5)	0.006±0.006	0.069±0.007	2.84	119.5±6.0	15–51	5.4	0.5	0.117±0.015	2.933	40.7±3.5	41.4±3.5
						5.4	1.0		2.848	42.0±3.6	
(4)	0.000±0.000	0.079±0.004	3.07	524.2±44.7	46–80	5.0	0.5	0.104±0.002	3.103	167.3±18.1	173.1±18.6
						5.0	1.0		3.048	172.0±18.6	
						10.0	0.5		3.048	172.0±18.6	
						10.0	1.0		2.892	181.3±19.6	
(3)	0.019±0.010	0.048±0.010	3.20	1028.8±128.4	8–41	4.0	0.5	0.0112±0.008	3.075	342.5±48.0	342.5±48.0

In the Comuzhelin basin, the North Comuzhelin fault (NCF) offsets stream risers and regressive lake shorelines left-laterally for ~50 m (Figs. 3 and 5). The current lake shoreline has an apparent 2500-m left-lateral offset across the fault, which may have resulted from an offset of paleo-topography. The North Comuzhelin fault also forms a linear ridge exposing bedrock; the ridge is dissected by north-flowing streams to form a series of water gaps. The fault surface cutting Quaternary alluvial deposits in an active stream channel displays subhorizontal striations on a nearly vertical fault surface (Fig. 7A).

The South Comuzhelin fault (SCF) is a sharp and linear topographic boundary (Fig. 3). It separates the Comuzhelin basin in the north from bedrock of the Tethyan Himalayan Sequence in the south. The fault truncates several alluvial fans but exhibits no clear evidence of left-lateral offsets. Thus, it is likely a dip-slip fault with the south side up. Determining if this fault is a thrust or normal fault has important implications for the active dynamics of the Himalayan orogen, but currently this information is not available due to the lack of direct exposure of the fault surface to determine its dip direction in the field.

5. Fault slip rates

5.1. Southern Gongzuo Fault

The Southern Gongzuo fault offsets a stream channel bounded by T2 and T3 terraces for ~3500 m (Fig. 4). Following Cowgill (2007), we used the oldest age of T3 unit at 3.4±0.5 Ma and the youngest age of T2 unit at 173.1±18.6 ka to determine the lower and upper bounds of fault slip rate at 1.0±0.1 mm/yr and 20.0±1.8 mm/yr, respectively. The above estimates assume that deposition of T2 surface stopped immediately after the start of fault offset. However, if deposition of the T2 surface continued during continuous fault motion, then the oldest age of T2 would be most representative for the actual slip rate. Using the oldest available age of 503.2±62 ka for the T2 unit, we obtain a much lower estimate of fault slip rate at 7.0±0.3 mm/yr for the upper bound.

5.2. Central Gongzuo Fault

The Central Gongzuo fault offsets an active channel bounded by T2b and T0 for ~1100 m (Fig. 4). Using the OSL age of 173.1±18.6 ka for the

erosion surface that lies at the base of the T2b unit, we obtained a slip rate of 6.4±0.6 mm/yr. Interpretation of this rate depends on whether deposition on the T2b surface has continued after the offset of the channel. Because T2b unit lies immediately next to an active and narrow stream channel, the stream may have spilled over the channel walls during periods of high fluxes, leaving younger deposits on top of the T2b surface. This scenario would make the above estimate of 6.4±0.6 mm/yr an upper bound for the actual slip rate of the Central Gongzuo fault.

5.3. North Gongzuo Fault

We have no direct geochronologic constraints on the slip rate of the North Gongzuo fault. If the development of major terraces was synchronous across the Gongzuo basin, then we may use the ages of the correlative terraces from the southern basin to estimate the slip rate of the fault. That is, the deposition age of the T3 terrace is 3.41 Ma, T2 is 503–173 ka, T1 is 41.4 ka, and T0 is 24.6 ka. A justification for this approach is that the terraces we have mapped are all fill terraces developed via punctuated climatic events (e.g., Bull, 1991). Keeping the above assumptions in mind, the inferred ages yield the following slip rates. For the offset of the T3–T2 riser, the slip rate has a lower bound of 0.1 mm/yr and an upper bound of 0.75–2.2 mm/yr. For the offset of the T2–T1 riser, the slip rate has a lower bound of 0.36–1.00 mm/yr and an upper bound of 4.4 mm/yr. For the offset of the T1–T0 riser, the slip rate has a lower bound of 2.1 mm/yr and an upper bound of 3.5 mm/yr. The above exercise indicates that the average slip rate on the North Gongzuo fault is about 2 mm/yr.

5.4. South and North Comuzhelin Faults

The North Comuzhelin fault offsets a regressive lake shoreline for about 50 m (Fig. 5). The shoreline deposits lie above an older alluvial fan sequence (unit Q1a and sample site 7 in Fig. 5) and below a lacustrine unit against the modern lake shoreline (sample site 8 in Fig. 5). The former yields an OSL age of 21.9±2.2 ka while the latter yields radiocarbon ages between 1290±55 yr and 3670±320 yr. Using these age constraints we obtain the lower and upper bounds of fault slip rate for the North Comuzhelin fault to be 2.3±0.2 mm/yr and 38.8±1.5 mm/yr, respectively. We have no constraint for the offset and slip rates on the South Comuzhelin fault. As discussed above, this structure could be a dip–slip fault and may not contribute to left-slip shear across the Dinggye area.

6. Discussion

6.1. Fault-slip rates and total slip magnitude

Our study suggests that the left-slip rates on individual faults in the eastern Himalaya vary from 1–2 mm/yr as the lower bound to

Table 3
Radiocarbon dating results

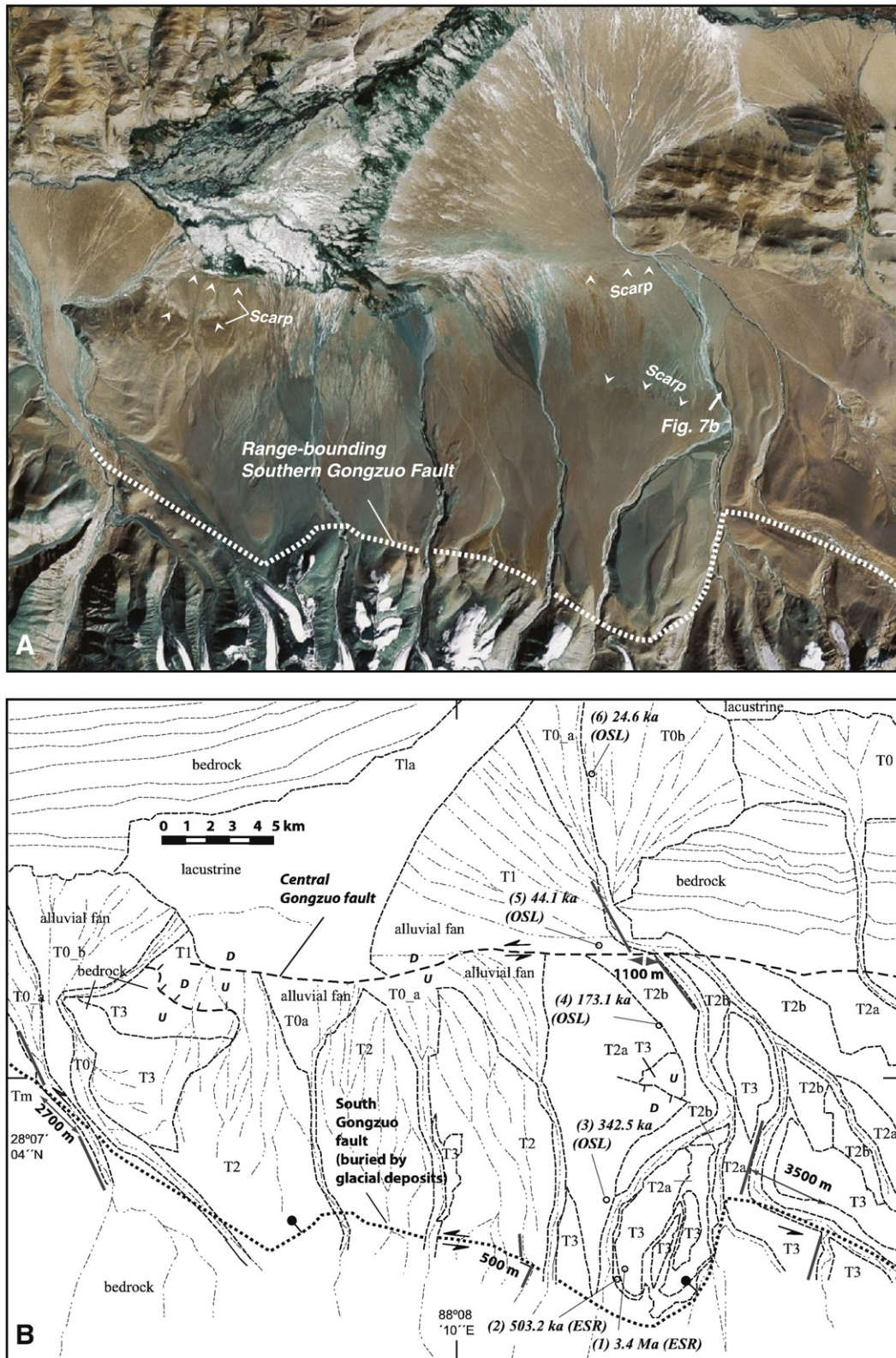| Sample number in Fig. 5	Lithology	Age (yr)	Tree-ring correction (calendar yrs BP)
(8a)	Clay	1290±55	1250±55
(8b)	Clay	3445±70	3690±100
(8c)	Clay	3670±320	3980±430

Fig. 4. (A) Google Earth image of the Central and Southern Gongzuo faults. (B) Interpreted Quaternary geologic map based on our field observations and interpretation of the above LANDSAT image. Map units: T0, most recent stream deposits; T1 to T3, younger to older Pliocene–Quaternary glacial, lacustrine, and alluvial deposits that form the capping sequences of various terraces. Location of age samples and associated dating methods are also indicated. OSL, age obtained from the optically stimulated luminescence method; ESR, age obtained from electron-spin-resonance optical dating method. "U" represents up-thrown fault block and "D" represents down-thrown fault block. The numbers in front of the ages sample locations listed in Tables 1–3 and discussed in the text. Location of Fig. 7B and its viewing direction are also shown.

6–39 mm/yr as the upper bound. As deposition on the offset terrace surfaces may have been continuous during fault motion, we consider the lower bounds to be more representative of the actual fault slip rates. Thus, the total left-slip shear rate across the four left-slip faults in the Dinggye area is 4–8 mm/yr. This rate is broadly compatible to those determined for the right-slip Karakorum fault in the western
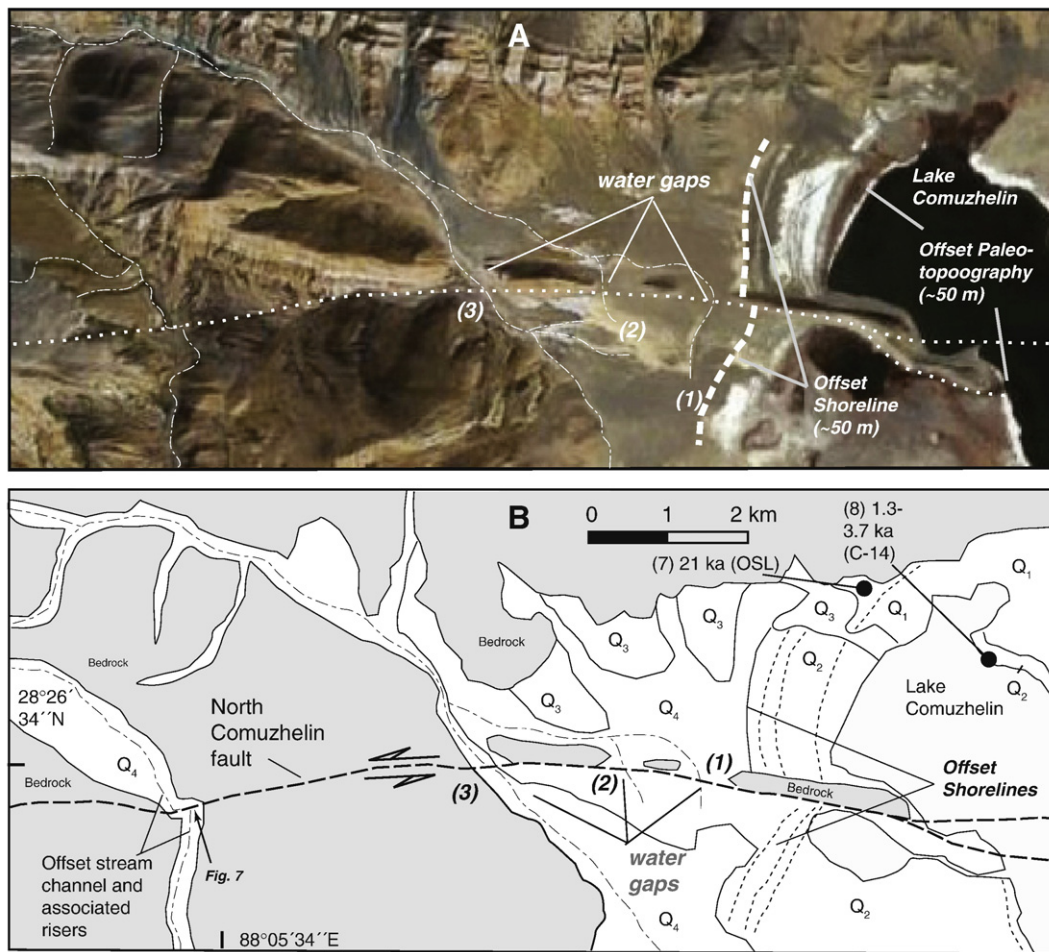
Fig. 5. (A) Google Earth image of the North Comuzhelin fault. (B) Four Quaternary units are mapped, with Q1 to Q4 from older to younger. Q1 represents the oldest fan deposits, Q2, lake shoreline deposits, Q3, young fan deposits postdating the regressive shorelines, and Q4, modern Quaternary alluvial deposits. Location of Fig. 7A and its viewing direction are also shown. OSL, age obtained from the optically stimulated luminescence method; C-14, age obtained from the carbon-14 method. The offset of the regressive lake shorelines, the arrangement of the water gap and the deflection of the drainage pattern, and the offset of river channels all indicate left-slip motion along the North Comuzhelin fault.

Himalayan arc at 1–10 mm/yr based on cosmogenic dating of offset Quaternary morphologic features and geodetic surveys (Brown et al., 2002; Wright et al., 2004; Chevalier et al., 2005; Valli et al., 2007). Because the left-slip faults we mapped are all located east of the middle point of the Himalayan arc (Fig. 1), their occurrence and slip rate are consistent with the oroclinal-bending model of Ratschbacher et al. (1992, 1994) for current deformation of the Himalayan arc (Fig. 1B).

Extrapolating the current mode of Himalayan-arc deformation back in time requires the knowledge of the initiation age and magnitude of total slip across the strike–slip systems in the Himalaya. In the western Himalaya, the right-slip motion on the Karakorum fault is 60–120 km starting at 25–10 Ma (Searle, 1996; Murphy et al., 2000; Phillips et al., 2004; Lacassin et al., 2004; Valli et al., 2007). Our study suggests that left-slip faulting in the eastern Himalaya must have occurred after 3–4 Ma, the oldest Pliocene unit offset by the left-slip faults (sample 1 from T3 unit in Fig. 4). However, we do not know the initiation age or the total magnitude of left-slip faulting in the eastern Himalaya. If the left-slip faults were initiated at the same time as the right-slip faults in the western Himalaya at 25–10 Ma and had maintained a constant slip rate as determined in this study, their total slip magnitude should also be in the range of 120–60 km. This inference is problematic when comparing the geometry of the strike–slip faults in the eastern and western Himalaya. In the west, the Karakorum fault is a single through-going structure, extending over 1000 km along strike (Fig. 1). This geometry indicates that the

Karakorum fault is capable of accommodating more slip than that by the short-segmented left-slip faults in the eastern Himalaya according to the global scaling law of fault displacement vs. fault length (e.g., Cowie and Scholz, 1992). If the slip rates have stayed constant for both the right-slip and left-slip faults in the Himalaya, the above argument requires the right-slip Karakorum fault to have initiated earlier than the left-slip faults in the eastern Himalaya. Alternatively, if the right-slip and left-slip faults started at the same time, the apparent larger slip on the Karakorum fault may imply a deceleration of its slip rate with time. In either case, the comparison of total fault slip suggests that right-slip faulting is more dominant than left-slip faulting in a finite-strain sense. This implies that eastward extrusion of western Tibet via right-slip faulting in the Himalayan arc was a dominant process in the earlier Himalayan history but became less important due to an increasing effect of oroclinal bending across the Himalayan arc later since 3–4 Ma when the left-slip faults began to develop in the eastern Himalaya.

A cautious note on the above discussion is that the short left-slip faults we studied are linked with long (>100–300 km) north-trending normal fault systems (Fig. 2), which complicates the use of the fault displacement vs. fault length scaling law that deals with straight faults with simple termination geometry (e.g., Cowie and Scholz, 1992). The connected geometry suggests that the left-slip faults serve as transfer structures between north-trending rifts, a relationship that has been also documented in central Tibet (e.g., Yin, 2000; Taylor et al., 2003) and western Mongolia (Bayasgalan et al., 2005; Walker et al., 2007).
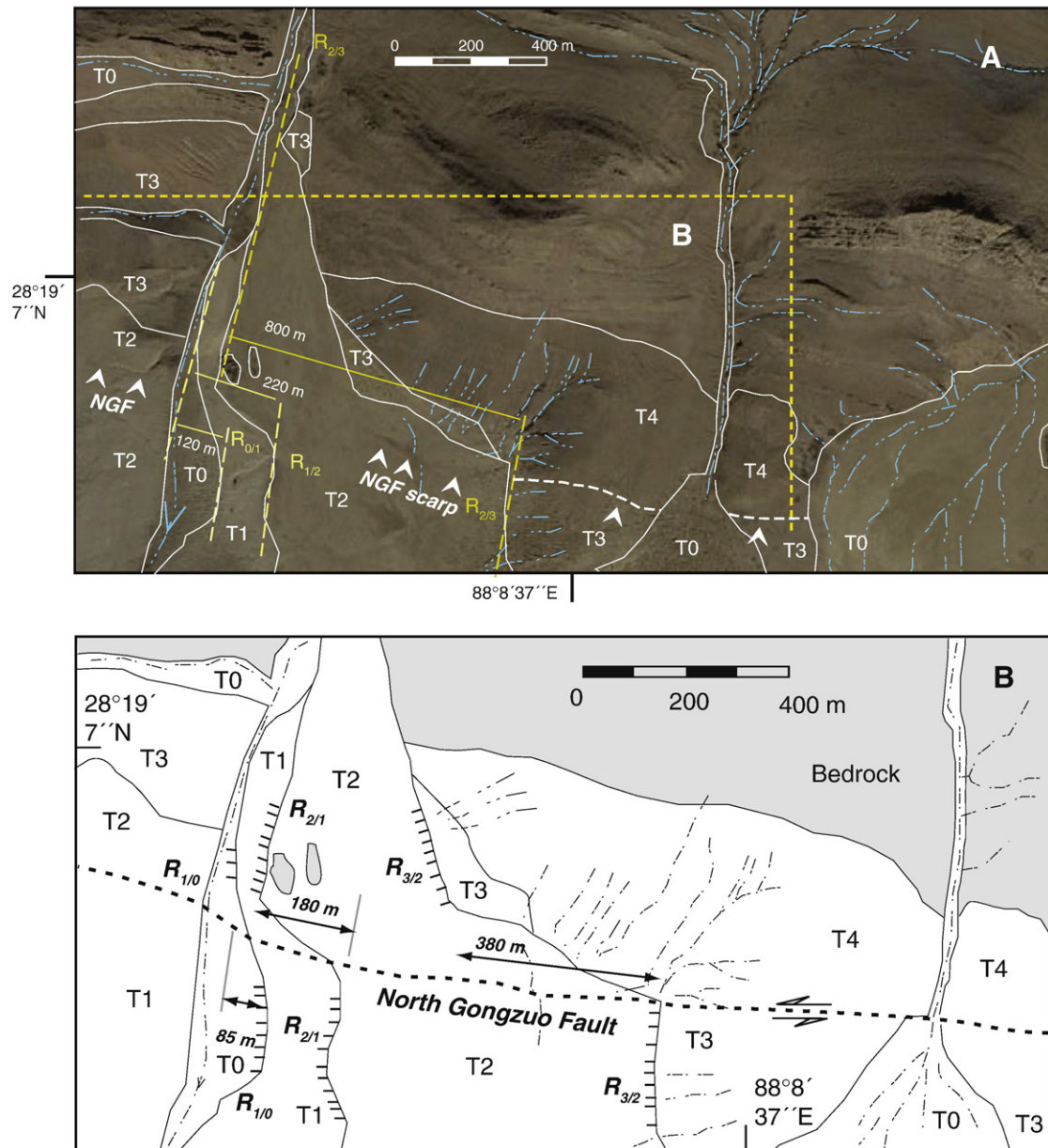
Fig. 6. (A) Google Earth image of the North Gongzuo fault (NGF). White arrows indicate the location of fault scarps observed in the field and shown on the satellite image. (B) Quaternary geologic map of the North Gongzuo fault based on our field observations and interpretation of the above satellite image. T0 to T4 are younger to older terrace deposits. $R_{1/0}$, $R_{2/1}$, and $R_{3/2}$ are older to younger stream risers offset left-laterally by the North Gongzuo fault.

6.2. Comparison with GPS data and focal-mechanism solutions

Although Cenozoic arc-parallel left-slip faulting has been recognized in the eastern Himalaya for over 15 years (e.g., Ratschbacher et al., 1994; Yin et al., 1994), our study is the first to document their Quaternary motion, Pliocene–Quaternary slip rates, and the timing of fault activities. Below, we compare the slip rates and fault kinematics obtained by our study to the available GPS data and focal mechanism solutions in our study area.

The existing GPS data across the central Himalayan arc are sparse and have high uncertainties in the range of 1.5 to 3.5 mm/yr (Paul et al., 2001) (Fig. 2). Two of the GPS velocity vectors of Paul et al. (2001) are used to estimate arc-parallel-shear and arc-perpendicular-shortening rates across our study area (stations (1) and (2) in Fig. 2). These velocity vectors yield a north-south shortening rate of 12± 3.0 mm/yr and an east-west left-slip shear rate of 2.5±1.5 mm/yr (i.e., 1–4 mm/yr). The left-slip shear rate from the GPS data overlaps our

lowest estimated slip rate of 4 mm/yr but is significantly below the upper bound of 8 mm/yr. The discrepancies may be due to several factors. First, the northern GPS station (station (1) in Fig. 2) is located west of a north-trending rift, against which the east-trending left-slip faults investigated by this study terminate. As a result, the differential motion between GPS stations (1) and (2) cannot capture accurately the slip rates across the left-slip faults. Second, the GPS velocity field could result from complex decay and accumulation of elastic strain over a broad region in between major earthquakes (e.g., Bilham et al., 1997; Feldl and Bilham, 2006). As a result, the decadal rate of deformation may not be comparable to the long-term geologic rate over thousands of years.

With regard to focal mechanisms, two recent strike–slip events in the lower crust in our study area indicate north-south contraction and east-west extension (events A and B in Fig. 2, from Priestley et al., 2007). The predicted orientation of the left-slip faults from the fault-plane solutions is in the northeast direction rather than the observed
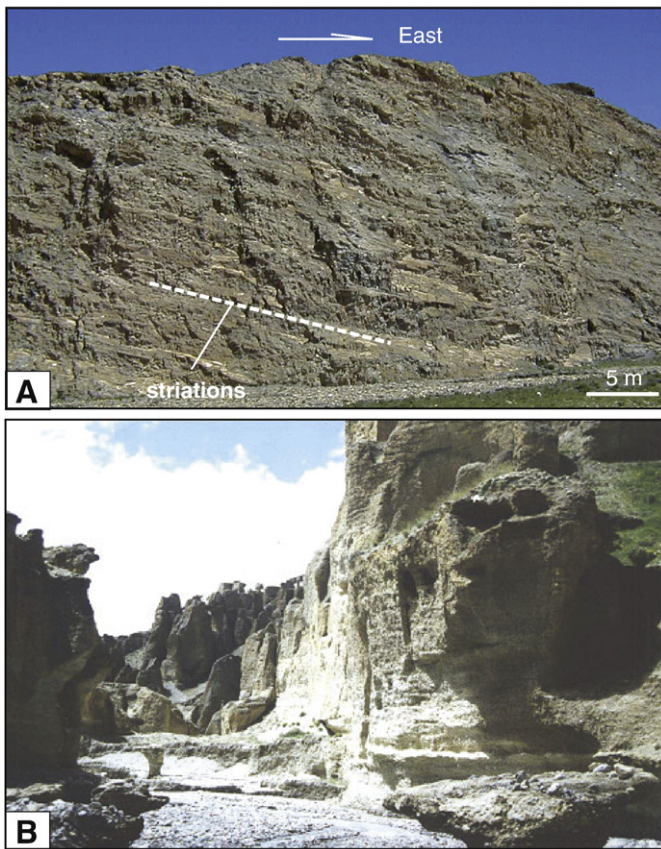
Fig. 7. (A) Subhorizontal striations on exposed near-vertical surface of the North Comuzhelin fault, viewed from the south. See Fig. 5 for location. (B) The fill T2 terrace in the southern Gongzuo Basin, viewed from south. See Fig. 4 for location.

east–west direction. This discrepancy could be explained by left-slip faulting occurring along reactivated pre-existing weakness (i.e., east-trending Tertiary thrusts in the THS and east-trending foliations in the GHC) (Yin, 2006) that may have very low coefficient of friction under north–south contraction (e.g., Mount and Suppe, 1987). Alternatively, the orientation of the strike–slip faults varies with depth, with lower crustal faults oriented in a northeast strike and the upper crustal faults oriented in an east strike.

The north-south convergence as indicated by both the GPS data and fault-plane solutions may help explain the observed vertical throw across all the studied left-slip faults in the study area. They suggest that the dip–slip components of the east-trending left-slip faults are most likely reverse-slip, accommodating active north-south shortening in the interior of the Himalaya.

6.3. Style and extent of the left-slip fault zone in the Eastern Himalaya

In addition to the east-trending basins examined in this study, we note that similar basins also exist farther to the east bounded by east-trending faults. When viewed together with the existing work of Ratschbacher et al. (1992, 1994) and Yin (1994), it appears that the distributed east-trending left-slip fault zone extends for >500 km from Dinggye (87°E) to Chigu Co (92°E) (i.e., the Dignnye–Chigu fault zone or DCFZ in Fig. 2). This broad left-slip shear zone may extend even farther to the east and link with the left-slip faults in the eastern syntaxis area as observed by Burg et al. (1998).

Distributed left-slip deformation in the eastern Himalaya is in sharp contrast to the discrete right-slip deformation in the western Himalaya (Fig. 1). It is possible that the different fault geometry results from a change in lithospheric rheology along the strike of the Himalayan arc. That

is, the western Himalaya is cooler and thus favors discrete deformation, whereas the eastern Himalaya was hotter and thus favors distributed deformation. This interpretation is not supported by the existing Pn velocity studies that indicate the eastern Himalaya to have a higher Pn velocity (~8.1 km s^{-1}) than that in the western Himalaya (7.9–8.0 km s^{-1}) (e.g., Liang and Song, 2006). This observation implies that the crust and possibly the whole lithosphere in the western Himalaya is hotter and weaker than in the eastern Himalaya, opposite to what one might expect from the above interpretation. Alternatively, the different fault geometry across the Himalayan arc may have resulted from different maturity of the fault systems, with the right-slip faults in the west developed first followed by the left-slip faults in the east. The older and thus more mature faults in the west exhibit discrete and through-going geometry whereas the younger and immature faults display short-segmented geometry. We may test this interpretation in the future by determining the initiation age of the left-slip faults in the eastern Himalaya. The best candidates for this purpose are the linked north-trending rifts whose exhumed footwall could yield useful age information about the timing of the rifts and thus the age of the linked strike–slip systems.

6.4. Temporally varying mechanisms for Himalayan-arc development

Three mechanisms may be responsible for the development of the Himalayan arc: continuum expansion, eastward extrusion, and oroclinal bending (Seeber and Armbruster, 1984; Amijo et al., 1986; Ratschbacher et al., 1992, 1994). The first two mechanisms lead to a decrease in arc curvature while the last mechanism leads to an increase in arc curvature. Eastward extrusion of western Tibet was a dominant process as indicated by the apparently greater amount of right-slip motion in the western Himalaya than that of left-slip motion in the eastern Himalaya. On the other hand, the comparable Pliocene–Quaternary slip rates in the western and eastern Himalaya suggest that oroclinal bending has become the dominant mechanism of Himalayan-arc deformation since 4 Ma. The above observations lead us to conclude that the arc-development mechanism in the Himalaya has varied temporally, with arc expansion (i.e., decreasing arc curvature) dominating in the earlier Himalaya history (from 25 Ma to 4 Ma) and arc contraction (i.e., increasing arc curvature) dominating in its recent history (from 4 Ma to the present).

The observed active radial convergence across the Himalayan front (Molnar and Lyon-Caen, 1989) suggests that continuum arc expansion is operating coevally with oroclinal bending. The synchronous occurrence of the two processes with opposite effects on the development of arc curvature is also expressed by the geometric linkage between the Himalayan strike–slip faults with north-trending rifts (Ratschbacher et al., 1994; Seeber and Pêcher, 1998; Murphy et al., 2000; Robinson et al., 2007). As strike–slip faults are the results of oroclinal bending while rifts are the results of continuum arc expansion, coeval occurrence of the two competing mechanisms suggests that the Himalayan arc may have achieved its dynamic balance that helps maintain a constant arc curvature. We can test this speculation in the future by determining the detailed rotational history of the eastern and western Himalayan arc using paleomagnetism.

7. Conclusions

This study together with the existing work reveals the presence of a ~100-km wide and >500-km long left-slip fault zone in the eastern Himalaya. The left-slip faults initiated after 4 Ma and have a total left-slip rate of 4–8 mm/yr across the 100-km fault zone. This rate is broadly comparable to the right-slip rate across the western Himalayan arc and supports the proposal that oroclinal bending is an important mechanism controlling active deformation of the Himalayan arc. As the total magnitude of right-slip faulting in the western Himalaya appears greater than that of left-slip faulting in the eastern Himalaya, it implies lateral extrusion and associated arc expansion leading to a decrease in arc curvature to be an dominant process in the

earlier history of the Himalayan arc development prior to ~4 Ma. In contrast, oroclinal bending has been a dominant mechanism of deformation across the Himalayan arc in the past 4 Ma. Although the role of oroclinal beding is to decrease the arc curvature, the linkage of Himalayan active strike–slip faults with north-trending rifts suggests that arc expansion and arc contraction are occurring in concert. The operation of the two mechanisms with opposing effects on arc curvature may be a result of dynamic equilibrium that helps maintain constant arc geometry. Due to the lack of information on the rotational history of the Himalayan arc and the initiation age of the left-slip faults in the eastern Himalaya, it remains unclear when and how this proposed dynamic equilibrium was achieved in the course of Himalayan-arc development.

Acknowledgements

References

Aitken, M.J., 1985. Thermoluminescence Dating. Academic Press, London.

Armijo, R., Tapponnier, P., Han, T., 1989. Late Cenozoic right-lateral strike–slip faulting in southern Tibet. J. Geophys. Res. 94, 2787–2838.

Bayasgalan, A., Jackson, J., McKenzie, D., 2005. Lithosphere rheology and active tectonics in Mongolia: relations between earthquake source parameters, gravity and GPS measurements. Geophys. J. Int. 163, 1151–1179.

Beerten, K., Stesmans, A., 2007. ESR dating of sedimentary quartz: possibilities and limitations of the single-grain approach. Quat. Geochronol. 2, 373–380.

Bilham, R., Larson, K., Freymueller, J., Project Idylhim, 1997. GPS measurements of present-day convergence across the Nepal Himalaya. Nature 386, 61–64.

Brown, E.T., Bendick, R., Bourles, D.L., Gaur, V., Molnar, P., Raisbeck, G.M., Yiou, F., 2002. Slip rates of the Karakorum fault, Ladakh, India, determined using cosmic ray exposure dating of debris flows and moraines. J. Geophys. Res. 107. doi:10.1029/2000JB000100.

Bull, W.B., 1991. Geomorphic Responses to Climatic Change. Oxford University Press, New York, p. 326.

Burchfiel, B.C., Chen, Z., Hodges, K.V., Liu, Y., Royden, L.H., Deng, C., Xu, J., 1992. The South Tibetan detachment system, Himalayan orogen. Extension contemporaneous with and parallel to shortening in a collisional mountain belt. Geological Society of America Special Paper, vol. 269, pp. 1–41.

Burg, J.P., Nievergelt, P., Oberli, F., Seward, D., Davy, P., Maurin, J.C., Diao, Z.Z., Meier, M., 1998. The Namche Barwa syntaxis: evidence for exhumation related to compressional crustal folding. J. Asian Earth Sci. 16, 239–252.

Chevalier, M.L., Ryerson, F.J., Tapponnier, P., Finkel, R.C., Van der Woerd, J., Li, H.B., Liu, Q., 2005. Slip-rate measurements on the Karakorum Fault may imply secular variations in fault motion. Science 307, 411–414.

Cowgill, E., 2007. Impact of riser reconstructions on estimation of secular variation in rates of strike–slip faulting: revisiting the Cherchen River site along the Altyn Tagh Fault, NW China. Earth Planet. Sci. Lett. 254, 239–255.

Cowie, P.A., Scholz, C.H., 1992. Displacement length scaling relationship for faults — data synthesis and discussion. J. Struct. Geol. 14, 1149–1156.

Ding, L., Zhong, D.L., Yin, A., Kapp, P., Harrison, T.M., 2001. Cenozoic structural and metamorphic evolution of the eastern Himalayan syntaxis (Namche Barwa). Earth Planet. Sci. Lett. 192, 423–438.

Feldl, N., Bilham, R., 2006. Great Himalayan earthquakes and the Tibetan plateau. Nature 444, 165–170.

Hutton, J.T., Prescott, J.R., 1992. Field and laboratory measurements of low-level thorium, uranium and potassium. Nucl. Tracks Radiat. Meas. 20, 367–370.

Klootwijk, C.T., Conaghan, P.J., Powell, C.M., 1985. The Himalayan arc: large-scale continental subduction, oroclinal bending, and back-arc spreading. Earth Planet. Sci. Lett. 75, 316–319.

Lacassin, R., Valli, F., Arnaud, N., Leloup, P.H., Paquette, J.L., Haibing, L., Tapponnier, P., Chevalier, M.L., Guillot, S., Maheo, G., Xu, Z.Q., 2004. Large-scale geometry, offset and kinematic evolution of the Karakorum fault, Tibet. Earth Planet. Sci. Lett. 219 (3–4), 255–269.

Li, D., 1992. On tectonic asymmetrical evolution of the Himalayan orogenic belt. Earth Sci. 17 (5), 539–540 (in Chinese with English abstract).

Liang, C.T., Song, X.D., 2006. A low velocity belt beneath northern and eastern Tibetan plateau from Pn topography. Geophys. Res. Lett. 33, L22306. doi:10.1029/2006GL027926.

Molnar, P., Lyon-Caen, H., 1989. Fault plane solutions of earthquakes and active tectonics of the Tibetan plateau and its margins. Geophys. J. Int. 99, 123–153.

Mount, V.S., Suppe, J., 1987. State of stress near the San Andreas fault — implications for Wrench Tectonics. Geology 15, 1143–1146.

Murphy, M.A., Yin, A., Kapp, P., Harrison, T.M., Lin, D., Guo, J.H., 2000. Southward propagation of the Karakoram fault system, southwest Tibet. Timing and magnitude of slip. Geology 28, 451–454.

Pan, G.T., Ding, J., Yao, D., Wang, L., 2004, Geological Map of Qinghai-Xiang (Tibet) Plateau and Adjacent Areas (1:1,500,000). Chengdu Institute of Geology and Mineral Resources, China Geological Survey, Chengdu Cartographic Publishing House, Chengdu, China.

Paul, J., Biirgrnann, R., Gaur, V.K., Bilham, R., Larson, K.M., Ananda1, M.B., Jade1, S., Mukal, M., Anuparna1, T.S., Satyal, G., Kumar, D., 2001. The motion and active deformation of India. Geophys. Res. Lett. 28, 647–650.

Phillips, R.J., Parrish, R.R., Searle, M.P., 2004. Age constraints on ductile deformation and long-term slip rates along the Karakoram fault zone, Ladakh. Earth Planet. Sci. Lett. 226, 305–319.

Prescott, J.R., Fox, P.J., 1993. Three-dimensional thermoluminescence spectra of feldspars. J. Phys., D, Appl. Phys. 26, 2245–2254.

Priestley, K., Jackson, J., McKenzie, D., 2007. Lithospheric structure and deep earthquakes beneath India, the Himalaya and southern Tibet. Geophys. J. Int. 172, 345–362 (2008).

Ratschbacher, L., Frisch, W., Chen, C., 1992. Deformation and motion along the southern margin of the Lhasa block (Tibet) prior to and during the India–Asia collision. J. Geodyn. 16, 21–54.

Ratschbacher, L., Frisch, W., Liu, G., Chen, C., 1994. Distributed deformation in southern and western Tibet during and after the India–Asia collision. J. Geophys. Res. 99, 19,817–19,945.

Robinson, A.C., Yin, A., Manning, C.E., Harrison, T.M., Zhang, S.H., Wang, X.F., 2007. Cenozoic evolution of the eastern Pamir: implications for strain-accommodation mechanisms at the western end of the Himalayan–Tibetan orogen. Geol. Soc. Amer. Bull. 119, 882–896.

Searle, M.P., 1996. Geological evidence against large-scale pre-Holocene offsets along the Karakoram Fault: implications for the limited extrusion of the Tibetan plateau. Tectonics 15, 171–186.

Seeber, L., Armbruster, J.G., 1984. Some elements of continental subduction along the Himalayan front. Tectonophysics 105, 263–278.

Seeber, L., Pêcher, A., 1998. Strain partitioning along the Himalayan arc and the Nanga Parbat antiform. Geology 26, 791–794.

Taylor, M., Yin, A., Ryerson, F.J., Kapp, P., Ding, L., 2003. Conjugate strike–slip faulting along the Bangong–Nujiang suture zone accommodates coeval east-west extension and north- south shortening in the interior of the Tibetan Plateau. Tectonics 22. doi:10.1029/2002TC001361.

Valli, F., Arnaud, N., Leloup, P.H., Sobel, E.R., Mahéo, G., Lacassin, R., Guillot, S., Li, H., Tapponnier, P., Xu, Z., 2007. Twenty million years of continuous deformation along the Karakorum fault, western Tibet: a thermochronological analysis. Tectonics 26. doi:10.1029/2005TC001913.

Walker, R.T., Nissen, E., Molor, E., Bayasgalan, A., 2007. Reinterpretation of the active faulting in central Mongolia. Geology 35, 759–762.

Wintle, A.G., 1997. Luminescence dating: laboratory procedures and protocols. Radiat. Meas. 27, 769–818.

Wright, T.J., Parsons, B., England, P.C., Fielding, E.J., 2004. InSAR observations of low slip rates on the major faults of western Tibet. Science 305, 236–239.

Yin, A., 2000. Mode of Cenozoic east-west extension in Tibet suggesting a common origin of rifts in Asia during the Indo–Asian collision. J. Geophys. Res. 105, 21745–21759.

Yin, A., 2006. Cenozoic tectonic evolution of the Himalayan orogen as constrained by along-strike variation of structural geometry, exhumation history, and foreland sedimentation. Earth-sci. Rev. 76, 1–131.

Yin, A., Harrison, T.M., Ryerson, F.J., Chen, W., Kidd, W.S.F., Copeland, P., 1994. Tertiary structural evolution of the Gangdese thrust system, southeastern Tibet. J. Geophys. Res. 99, 18,175–18,201.